AIMS Materials Science, 8(6): 974–989.
DOI: 10.3934/matersci.2021059
Received: 11 August 2021
Accepted: 16 December 2021
Published: 21 December 2021

http://www.aimspress.com/journal/Materials

*Research article*

# Incorporation of zirconium into PEO coating on Ti6Al4V alloy from acidic electrolyte

**Jie Sun[1],*, Tzvetanka Boiadjieva-Scherzer[1] and Hermann Kronberger[2]**

[1] Centre of Electrochemical Surface Technology GmbH (CEST GmbH), Austria
[2] Technical University of Vienna, Institute of Chemical Technologies and Analytics, Austria

* **Correspondance**: Email: jie.sun@tuwien.ac.at.

**Abstract:** To imitate the superior biocompatibility of Ti–Zr alloys at reduced cost, conventional Ti6Al4V alloy was modified via plasma electrolytic oxidation (PEO). The influence of different additives on the phase composition and topography was investigated in acidic electrolytes containing $Zr(SO_4)_2 \cdot H_2O$ with potentiostatically controlled PEO at different pulse frequencies. Apart from the primary intention to generate Zr enriched phases, formation and incorporation in the ceramic layer of potential antibacterial Cu and Zn species was achieved and examined by X-ray diffraction. The thickness of the oxide layer, the adhesion and the layers' composition were evaluated using FIB and SEM-EDX.

**Keywords:** plasma electrolytic oxidation; Ti6Al4V alloy; biomaterial; titanium, zirconium; copper; zinc; surface modification

## 1. Introduction

For biological hard tissue replacement, development of biomaterials focuses on increase of biocompatibility while maintaining required mechanical properties. In vivo studies have revealed that Ti–Zr alloy- and Zr outperform Cr- and Ti-implants with the Ti–Zr alloys triggering the lowest tissue responses and sensitization [1,2]. The biological response at the biomaterial-host interface is mediated by the chemical composition of the passive film [3]. $ZrO_2$ has superior mechanical strength and hardness compared to Ti [4] and is considered biocompatible with high affinity for bone tissue [5,6]. $TiO_2$ is known for its osteogenic effect [7]. Herein, the combination of both materials could diminish their deficiencies. Compared with $TiO_2$ ceramic, sintered composites of $ZrO_2$–$TiO_2$

induce faster cell attachment and proliferation assumingly due to presence of solid solutions [8]. One possible disordered solid solution is zirconium titanate, which positively affects human cell viability [9–11]. Preparation of zirconium titanate ceramics involves powder synthesis via solid state reactions, high energy ball milling, co-precipitation, sol-gel or mechanochemical processing and includes subsequent pressing and sintering [12].

On the contrary, surface modification methods preserve the structural support, ductility and impact resistance of the metallic bulk material while producing ceramic coatings with superior corrosion resistance, biocompatibility and reduced thermal conductivity/expansion. In contrast to physical [13] or chemical vapor deposition [14], plasma electrolytic oxidation (PEO) is a less expensive and a faster treatment. During the PEO process, high voltage initializes rapid growth of dielectric layers on the polarized metal, followed by breakdown and plasma discharge processes [15,16]. Simultaneously, metal dissolution occurs, while the electrolyte is ionized, enabling ion incorporation and/or particle absorption in the growing oxide layer [17–19]. Both the topography and phase composition of the ceramic layer are controlled by current density, applied voltage, frequency, duty cycle and electrolyte formulations.

For biomedical applications, PEO parameters are selected to create porous micro-topographies for increased contact area and formation of phases contributing to the biocompatibility [20]. Most PEO research groups modify Ti in phosphate/silicate electrolytes to enrich the oxide layer with phosphate and silicate with polarizations up to 500 V [21,22]. A different PEO approach is incorporation of Zr enriched particles in alkaline baths. High pH prevents dissolution of $ZrO_2$ particles, while evaporation of the solution immobilizes, and the sparking event sinters them to the surface. Additives like $ZrF_2$ led in presence of phosphates predominantly to the formation of $KZr_2(PO_4)_3$ with minor traces of $ZrO_2$ and $ZrP_2O_7$ [23]. Whereas addition of $ZrO_2$ nanoparticle to the bath composition resulted in particle incorporation [24,25].

Research on binary Ti–Cu [26], ternary alloy systems like Ti–xCu–yMn alloys [27] and thermodynamic assessment of the system Cu–Ti–Zr [28] indicate potential incorporation of antibacterial metals. Rokosz et al. fabricated porous coatings enriched in copper on a ternary Ti–Nb–Zr alloy by PEO in a bath containing $H_3PO_4$ and $Cu(NO_3)_2$ in a potential range of 180 and 450 V. EDX data show less than 3 mass% Zr due to alloy composition but up to 9.2 mass% Cu [29]. Even though high Cu concentration achieves bacterial biofilm suppression, its high cytotoxicity also reduces the biocompatibility [30]. Herein, low antibacterial metal incorporation is tolerable.

The current work focuses on the formation of Zr phases similar to biocompatible $ZrTiO_4$ [9] in dependence of metal ion additives (Zr, Zn, Cu) and varying pulse parameters but also evaluates the incorporation of these metals within the PEO coatings.

## 2. Materials and methods

Commercial Ti6Al4V samples were ground, polished (P220, P400 and P1000), rinsed with distilled water and ethanol. A surface area of ~6 $cm^2$ was submersed in the electrolytes and treated for 10 min in a two-electrode configuration with varying pulse frequencies at different voltages and electrolyte compositions. The electrolyte contained 0.12 M $Zr(SO_4)_2 \cdot H_2O$ dissolved in 0.1 M $H_2SO_4$ and either 0.03 M $ZnSO_4 \cdot 7H_2O$ or 0.03 M $Cu(CH_3COO)_2 \cdot H_2O$. As a cathode a steel coil was used, and a cooling pipe was connected with a heat exchanger to maintain bath temperatures at 20 °C. The

potentiostatic pulses were applied with the power supply *Power Station pe3000-8*. An overview of the PEO experiments is presented in Table 1.

Specimens were further investigated via FIB, SEM and EDX. All samples were qualitatively and semi-quantitatively examined via XRD using Rietveld refinement.

**Table 1**. Overview of PEO experiments.

| Electrolyte formulation | Potential (V) | Pulse frequency (Hz) | Duty cycles (%) |
|---|---|---|---|
| 0.1 M $H_2SO_4$, 0.12 M $Zr(SO_4)_2 \cdot H_2O$ | 100 | 0.011 | 67 |
| 0.1 M $H_2SO_4$, 0.12 M $Zr(SO_4)_2 \cdot H_2O$ | 150 | 0.011 | 67 |
| 0.1 M $H_2SO_4$, 0.12 M $Zr(SO_4)_2 \cdot H_2O$ | 200 | 0.011 | 67 |
| 0.1 M $H_2SO_4$, 0.12 M $Zr(SO_4)_2 \cdot H_2O$, 0.03 M $ZnSO_4 \cdot 7H_2O$ | 100 | 0.011 | 67 |
| 0.1 M $H_2SO_4$, 0.12 M $Zr(SO_4)_2 \cdot H_2O$, 0.03 M $ZnSO_4 \cdot 7H_2O$ | 125 | 0.011 | 67 |
| 0.1 M $H_2SO_4$, 0.12 M $Zr(SO_4)_2 \cdot H_2O$, 0.03 M $ZnSO_4 \cdot 7H_2O$ | 150 | 0.011 | 67 |
| 0.1 M $H_2SO_4$, 0.12 M $Zr(SO_4)_2 \cdot H_2O$, 0.03 M $Cu(CH_3COO)_2 \cdot H_2O$ | 100 | 0.011 | 67 |
| 0.1 M $H_2SO_4$, 0.12 M $Zr(SO_4)_2 \cdot H_2O$, 0.03 M $Cu(CH_3COO)_2 \cdot H_2O$ | 125 | 0.011 | 67 |
| 0.1 M $H_2SO_4$, 0.12 M $Zr(SO_4)_2 \cdot H_2O$, 0.03 M $Cu(CH_3COO)_2 \cdot H_2O$ | 150 | 0.011 | 67 |
| 0.1 M $H_2SO_4$, 0.12 M $Zr(SO_4)_2 \cdot H_2O$, 0.03 M $Cu(CH_3COO)_2 \cdot H_2O$ | 150 | 10 | 50 |
| 0.1 M $H_2SO_4$, 0.12 M $Zr(SO_4)_2 \cdot H_2O$, 0.03 M $Cu(CH_3COO)_2 \cdot H_2O$ | 150 | 50 | 50 |
| 0.1 M $H_2SO_4$, 0.12 M $Zr(SO_4)_2 \cdot H_2O$, 0.03 M $Cu(CH_3COO)_2 \cdot H_2O$ | 200 | 0.011 | 67 |
| 0.1 M $H_2SO_4$, 0.12 M $Zr(SO_4)_2 \cdot H_2O$, 0.03 M $Cu(CH_3COO)_2 \cdot H_2O$ | 200 | 10 | 50 |
| 0.1 M $H_2SO_4$, 0.12 M $Zr(SO_4)_2 \cdot H_2O$, 0.03 M $Cu(CH_3COO)_2 \cdot H_2O$ | 200 | 50 | 50 |

### *2.1. Scanning electron microscopy (SEM), energy-dispersive X-ray (EDX) spectroscopy, focused ion beam (FIB)*

Sample imaging via scanning electron microscopy (SEM) was carried out with a ZEISS Sigma HD-VP FE-SEM (Field Emission) equipped with a Schottky field emission source for increased spatial resolution.

The chemical composition of the surface was determined using the coupled energy-dispersive X-ray (EDX) detector EDAX-TEAM OCTANE PLUS SDD. EDX measurements were performed as integral area scans on the top surfaces and on the cross-sections with spot analysis (to avoid concealment by the substrate's signal) for detection of Zr, Zn and Cu.

For preparation of high-quality cross-sections, a Quanta 200 3D by FEI, a dual beam machine with a traditional thermal emission SEM combined with a focused ion beam (FIB) cannon using a Gallium LIMS-Liquid ion metal source was used. Initially, a protective Pt layer of 500 nm was sputtered solely onto the cutting area by injecting an organic Pt-complex into the ion beam. A rough cut with higher beam current is followed by a fine cut with low beam current creating a smooth cross-section.

### *2.2. X-ray diffractometry (XRD)*

The phase composition of PEO treated specimens was determined with a Philips X'Pert powder diffractometer equipped with a Cu X-ray tube (operated at 45 kV and 40 mA), an automated divergence slit, a graphite monochromator, and a scintillation counter. The receiver slit was 0.1 mm

(2θ = 0.033°) with an anti-scatter slit of 4° and a Soller slit of 0.04 rad on both sides of the sample. Measurements were conducted in continuous mode for the 2θ range from 5 to 110° with 0.05° increments. Phase composition identification and calculation of the shares were performed via iterative Rietveld refinement. Phase quantification was only carried out with the main Zr and Ti phases excluding traces of Zn and Cu phases to avoid misinterpretation due to amounts below XRD detection limit rendering the pattern susceptible to inferences caused by overlap of multiple patterns.

## 3. Results and discussion

### *3.1. Plasma electrolytic oxidation of Ti6Al4V in $H_2SO_4$ in presence of Zirconium additive*

In dependence of the electrolyte composition, different tendencies of particle formation are present. During the anodic polarization, the substrate is dissolving. Ions from the electrolyte are immobilized within the molt by rapid quenching and evaporation of the solution in the vicinity of the sparking sample. Simultaneously, dissolved metal ions form precipitates, incorporating into the growing oxide layer.

In absence of zirconium additive, $TiO_2$-rutile is the dominating $TiO_2$ phase produced by PEO treatments in a sulfuric acid solution [20]. In presence of zirconium sulfate as additive, Rudnev et al. characterized tetragonal and monoclinic $ZrO_2$ fractions within the grown oxide layer [31]. In contrast to their findings, a different phase yield in our study: $Zr_{0.35}Ti_{0.65}O_2$ which is a result of differences in pulse parameters and bath composition. The phase srilankite $Zr_{0.35}Ti_{0.65}O_2$ is a high-temperature disordered phase crystallizing in the orthorhombic α-$PbO_2$ structure. Formation of srilankite has been reported at 800 °C when annealing the alloy Ti–15Zr–4Ta–4Nb [32]. $Zr_{0.35}Ti_{0.65}O_2$ is stable above 1100 °C and remains metastable at lower temperature due to sluggish ordering processes associated with reconstructive transformation and driven by the preferred coordination of Ti and Zr ions [33]. While, little research exists on srilankite's interaction with biological systems, literature indicates biocompatibility of zirconium titanate [9], another modification stable below 1200 °C [34]. Both modifications are disordered $(Ti,Zr)O_2$ solid solutions [32] and assumingly exhibit similar biocompatibility. $ZrTiO_4$ powder crystallizes at 580 °C and is fully transformed at 700 °C [35]. Whereas $TiO_2$-anatase to rutile transition commences at 400 °C and is fully transformed at 700 °C [36]. With rising temperature, a cascade of possible phase formations occurs. High sparking temperatures result in omitting the formation of $TiO_2$-anatase. Herein, $TiO_2$-rutile is the dominant phase at relatively lower voltages and higher frequencies due to less accumulated heat and time for phase transition but closely followed by formation of $Zr_{0.35}Ti_{0.65}O_2$ at higher polarizations and longer pulses.

For defining of the working window and as a reference system, Ti6Al4V specimens were polarized in 0.1 M sulfuric acid containing 0.12 M $Zr(SO_4)_2 \cdot H_2O$ with potentials of 100, 150 and 200 V. During the PEO treatment, simultaneous anodic dissolution of the substrate material and oxidation take place. With increasing the polarization voltage, clouding of the electrolyte intensified.

XRD patterns (Figure 1a,b) of specimens treated at 100 V and 150 V indicate increasing fraction of tetragonal $TiO_2$-rutile and orthorhombic $Zr_{0.35}Ti_{0.65}O_2$ with rising potentials (Table 2). The surface morphology of the specimens obtained at the different voltages is shown in Figure 2. The dominance of $TiO_2$-rutile in the phase composition (Figure 1b) could be related to particle absorption leading to protruding microstructures (Figure 2b). While at 100 V, 10.1% $Zr_{0.35}Ti_{0.65}O_2$ is

formed, 30.2% $TiO_2$-rutile is generated at 150 V. The phase composition fabricated at 150 V exhibits no substrate pattern indicating a dense ceramic coating. Further increase of polarization to 200 V led to partial detachment of the oxide layer during sparking events, but enabled formation of uniformly distributed pores (Figure 2c). The corresponding XRD pattern (Figure 1c, Table 2) shows mainly the pattern of the underlying substrate (93.9%) with 6.1% $Zr_{0.35}Ti_{0.65}O_2$. This porous topography appears interesting for biomedical application but is accompanied by material loss through detachment and increased substrate dissolution at the high polarization potential.

The baselines of the XRD patterns bend by 10 to 12° in the range of 20–40°2θ relative to the flat baseline are related to amorphous $TiO_2$ and $ZrO_2$. Calculations in the Rietveld refinement exclude the amorphous fraction and therefore evokes the incorrect impression of low PEO coating formation. For crystalline phase compositions enriched with Zr and less $TiO_2$-rutile phase, more intense sparking events are required to generate localized heat but simultaneously detachment of the coating needs to be prevented. Hence, the influence of additives to alter the oxide growth with the preference to generate $Zr_{0.35}Ti_{0.65}O_2$ was investigated.

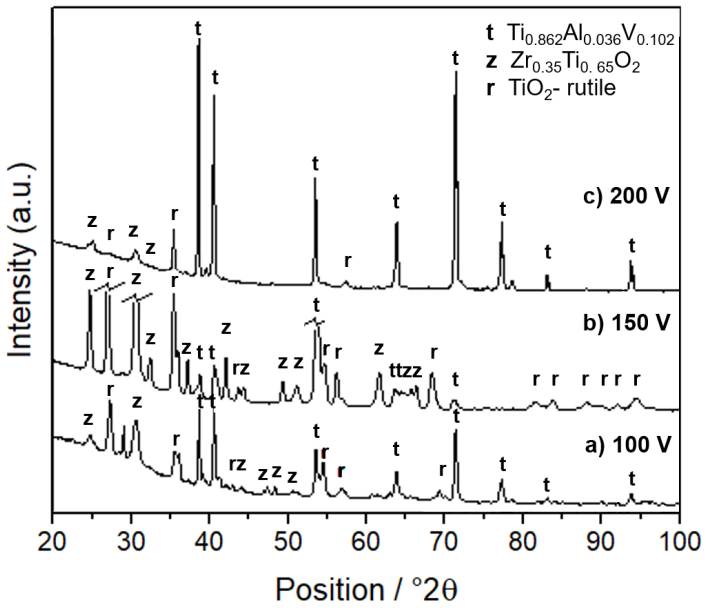


**Figure 1.** XRD patterns of Ti6Al4V treated by PEO in 0.1 M sulfuric acid containing 0.12 M $Zr(SO_4)_2 \cdot H_2O$ at different voltages.

**Table 2**. Quantification of phase composition via Rietveld refinement corresponding to Figure 1.

| Potential (V) | $Ti_{0.862}Al_{0.036}V_{0.102}$ (%) | $Zr_{0.35}Ti_{0.65}O_2$ (%) | $TiO_2$-rutile (%) |
|---|---|---|---|
| 100 | 59.1 | 10.1 | 30.8 |
| 150 | - | 30.2 | 69.8 |
| 200 | 93.9 | 6.1 | - |

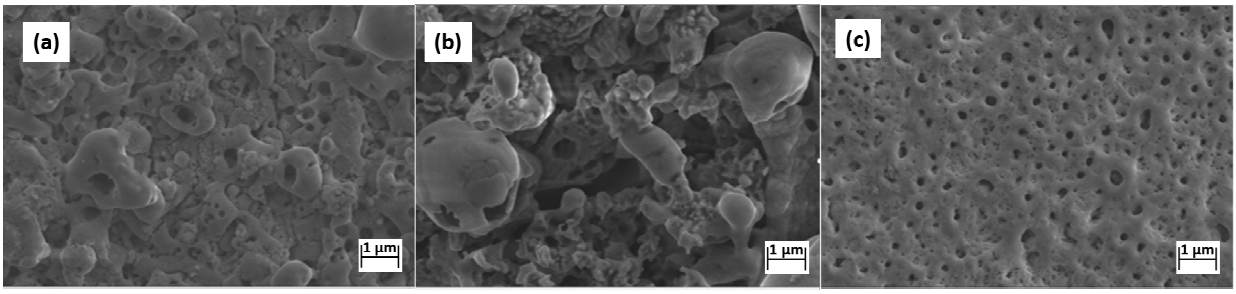


**Figure 2.** SEM images of Ti6Al4V treated by PEO in 0.1 M sulfuric acid containing 0.12 M $Zr(SO_4)_2 \cdot H_2O$ at different voltages of (a) 100, (b) 150 V and (c) 200 V.

### *3.2. Influence of metal ion additives on the phase composition*

Addition of zinc sulfate slightly reduced the particle formation in the electrolyte during the PEO. From 100 to 125 V, only small fractions of $TiO_2$-rutile (0.6%) and $Zr_{0.35}Ti_{0.65}O_2$ (3.1%) were formed. At 125 V, $TiO_2$-rutile was the dominant $TiO_2$ phase (31.2%). At 150 V, intensified sparking events enabled sintering of particles into the surface enriching the grown oxide layer further with $TiO_2$-rutile. With increasing potential, the continuous decrease of substrate pattern and its disappearance at 150 V show the formation of denser oxide layer accompanied by increasing Zr incorporation. In presence of zinc additive, the $Zr_{0.35}Ti_{0.65}O_2$ to $TiO_2$-rutile ratio obtained by polarization with 150 V is shifted to the Zr enriched phase (49.4%). Nearly equal proportions of $TiO_2$-rutile and $Zr_{0.35}Ti_{0.65}O_2$ were produced at 150 V showing that both phase formations require similar intense discharges and temperatures for the phase formations. While white clouding of the bath intensified with polarization voltage, the tendency of $TiO_2$ particle formation and their subsequent absorption increased. Absence of the substrate pattern at 150 V (Figure 3c, Table 3) indicates that the as-prepared ceramic layer is dense and further increase of voltage would lead to undesired layer detachment by dielectric breakdown events as encountered without zinc additive (Figure 2c, Table 3). Formation of amorphous $TiO_2$ and $ZrO_2$ leads to tilting the baseline of the XRD patterns in the range of 20–40°2θ by an angle of 8 to 9°.

The zinc additive gave rise of a new phase, cubic $Zn_{0.5}V_2O_4$ (Figure 3, Table 3). In the acidic bath, the anodic polarization caused leaching of the less corrosion resistant alloying element V which reacts with available Zn ions forming $Zn_{0.5}V_2O_4$. High release rates of V could exhibit adverse effects on health [37] but is relatively benign at low concentrations as it is an essential nutrient [38]. The PEO generated $Zn_{0.5}V_2O_4$ has potential to exhibit antibacterial activity since research on $ZnV_2O_5$ indicate antibacterial activity against *E.coli* and *S. aureus* [39].

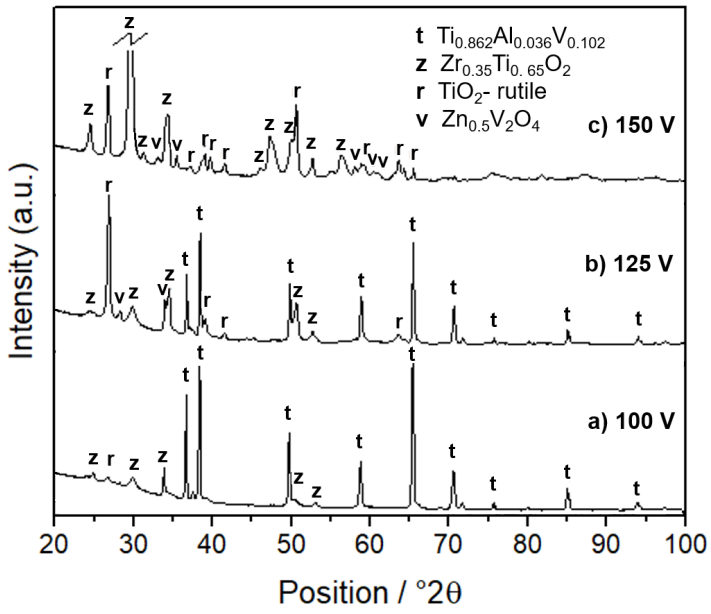


**Figure 3.** XRD patterns of Ti6Al4V treated by PEO in 0.1 M sulfuric acid containing 0.12 M $Zr(SO_4)_2 \cdot H_2O$ and 0.03 M $ZnSO_4 \cdot 7H_2O$ at different voltages.

**Table 3.** Quantification of phase composition via Rietveld refinement corresponding to Figure 3.

| Potential (V) | $Ti_{0.862}Al_{0.036}V_{0.102}$ (%) | $Zr_{0.35}Ti_{0.65}O_2$ (%) | $TiO_2$-rutile (%) |
|---|---|---|---|
| 100 | 96.2 | 3.1 | 0.6 |
| 125 | 67.6 | 1.1 | 31.2 |
| 150 | - | 49.4 | 50.6 |

SEM images show uniformly distributed pores formed at 100 V (Figure 4a). With increasing voltage, at 125 V, the surfaces' smoothness decrease and exhibit protruding structures with less homogenous distributed small pores (Figure 4b). The micro-topography exhibits no cracks and is uniformly covered with pores with up to 500 nm. At 150 V, spherical features indicate particles fused into the surface. The topography exhibits micro-cracks of up to 5 µm (Figure 4c).

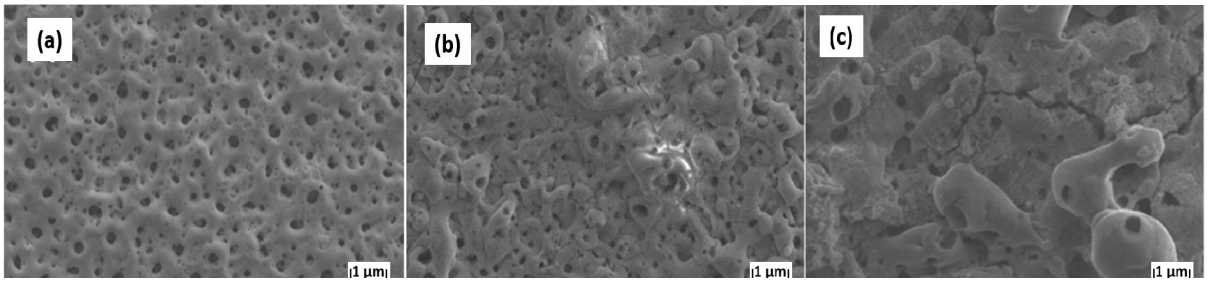


**Figure 4.** SEM investigation of Ti6Al4V treated by PEO in 0.1 M sulfuric acid containing 0.12 M $Zr(SO4)_2 \cdot H_2O$ and 0.03 M $ZnSO_4 \cdot 7H_2O$ at different voltages: (a) 100 V, (b) 125 V and (c) 150 V.

Addition of copper acetate to the sulfuric zirconium bath altered the trend and ratio of polarization dependent phase composition (Figure 5, Table 4) to the preferred $Zr_{0.35}Ti_{0.65}O_2$ phase. The polarization of 100 V generated mild sparking events leading to low concentrations of both $TiO_2$-rutile and $Zr_{0.35}Ti_{0.65}O_2$. At 125 V, the dominant oxide phase is constituted of $TiO_2$-rutile (28.6% and only 4% $Zr_{0.35}Ti_{0.65}O_2$) and fully replaced by $Zr_{0.35}Ti_{0.65}O_2$ at higher voltages of 150 (36.9%) and 200 V (80.7%).

With the increase of the polarization voltage, XRD patterns indicate increased formation of anorthic $Cu_2V_2O_7$ (Figure 5b–d) by reaction of copper ions with vanadium ions leeched from the substrate, similar to $Zn_{0.5}V_2O_4$. In contrast to the influence of zinc sulfate on the bath, copper acetate led to a transparent blue solution and prevented formation of a suspension during polarization. Partial copper deposition was observed at the steel cathode with and without polarization due to cathodic deposition and cementation, but the electrolyte remained clear and intensely blue indicative for available Cu species. The formation of different oxide species at the sample surface involved mainly element incorporation by immobilizing ions through evaporation of the electrolyte. In contrast to sole Zr additive or combined with Zn addition, a gradual decline of amorphous $TiO_2$ and $ZrO_2$ is apparent in the XRD patterns by the disappearance of the bending angle in the range of 20–40°2θ (at 100 V 8°, at 125 V 7° and ≥150 V none).

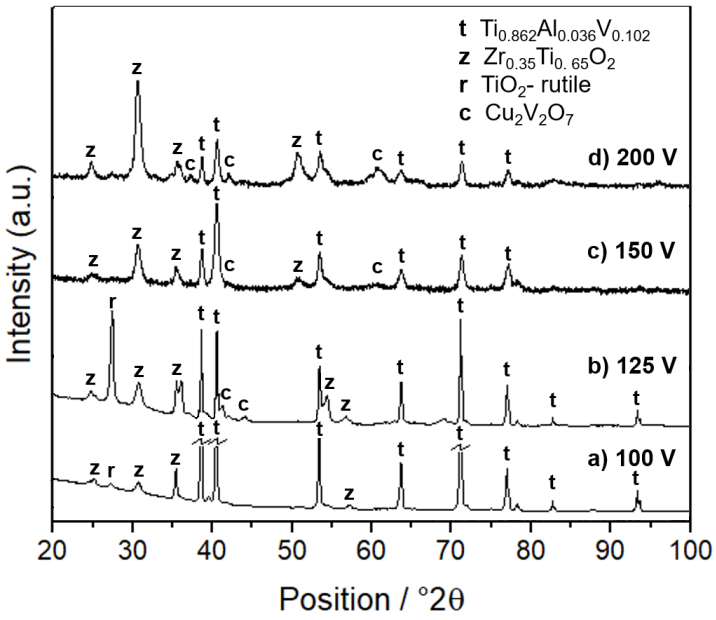


**Figure 5.** XRD patterns of Ti6Al4V treated by PEO in 0.1 M sulfuric acid containing 0.12 M $Zr(SO_4)_2 \cdot H_2O$ and 0.03 M $Cu(CH_3COO)_2 \cdot H_2O$ at voltages of (a) 100 V, (b) 125 V, (c) 150 V and (d) 200 V.

**Table 4.** Quantification of phase composition via Rietveld refinement corresponding to Figure 5.

| Potential (V) | $Ti_{0.862}Al_{0.036}V_{0.102}$ (%) | $Zr_{0.35}Ti_{0.65}O_2$ (%) | $TiO_2$-rutile (%) |
|---|---|---|---|
| 100 | 97.6 | 1.1 | 1.3 |
| 125 | 67.3 | 4.0 | 28.6 |
| 150 | 63.2 | 36.9 | - |
| 200 | 19.3 | 80.7 | - |

SEM imaging (Figure 6) show the influence of increase of the polarization voltage on the topology. At 100 V, homogenous distributed pores below 500 nm diameters covered the surface with a high pore density. At 125 V, protruding structures were formed. With further increased polarization, small pores were fused together forming fewer slightly larger pores as discharge channels. The topography smoothened at 150 V due to molt formation and decrease of pore size. The most distinct topography change occurred at 200 V when quenching of the molt led to less uniformly distributed pores.

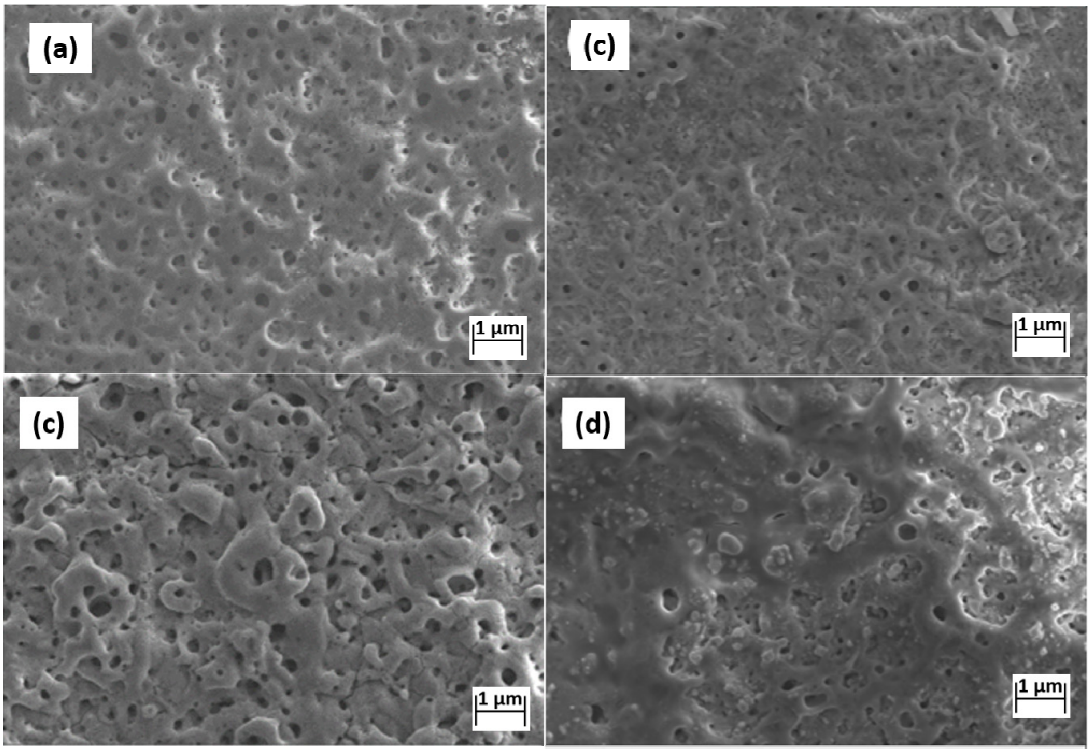


**Figure 6.** SEM investigation of Ti6Al4V treated by PEO in 0.1 M sulfuric acid containing 0.12 M $Zr(SO_4)_2 \cdot H_2O$ and 0.03 M $Cu(CH_3COO)_2 \cdot H_2O$ at different voltages: (a) 100 V, (b) 125 V and (c) 150 V and (d) 200 V.

### *3.3. Influence of pulse frequency and additives*

Conventional pulsed PEO treatments focus on high frequencies with pulse durations of a few milliseconds to form dense oxide layers for corrosion resistance. While the total area of micro-discharge decreases with frequency, reducing layer growth, the voltage range is limited for the PEO process conducted at low frequency. Undesired arcs disrupting the compact oxide layer can be reduced at high pulse frequencies [40]. Typically used pulse frequencies are above 50 Hz with varying duty cycles [21]. Shortening the discharge event allows the molten oxides to collapse into the discharge channel leading to denser, less porous layers. On the contrary, many PEO treatments of Ti-based alloys for biomedical applications intentionally generate porosity to positively affect the cells proliferation. The pore formation is also driven by gas evolution during local heating, melting and vaporization within the coating creating cavities [41]. The choice of pulsed PEO with constant voltage or current is dependent on the substrate and highly influences the surface structure. Constant

current enforces more violent breakdown events potentially deteriorating the grown oxide layer. Subsequent constant voltage oxidation partially repairs defects within the coating [42].

In the present work, the chosen pulsing parameter of 1 s long pulses of constant voltage with 0.5 s down time, equals to 0.011 Hz with a duty cycle of 67% is rather unconventional and a mixture of constant voltage polarization and pulsing. The long pulse duration delays quenching of the molt allowing local heat accumulation for formation of high temperature phases like $Zr_{0.35}Ti_{0.65}O_2$. Regularity of the coatings and in-depth surface to substrate morphology is characteristic for all the layers. The FIB cuts indicate good coatings-substrate adhesion. The coatings' thickness was determined and is discussed in the following paragraphs.

Specimens anodized in 0.1 M $H_2SO_4$ and 0.12 M $Zr(SO_4)_2 \cdot H_2O$ were prepared as a reference system for investigation of the influence of additional additives on the growth of the ceramic coating. Sample produced at 100 V and 0.011 Hz was selected for a FIB cut (Figure 7a) due to better coating adhesion compared to samples anodized at 150 V and 200 V. The coating thickness is 0.93 µm and homogenously distributed (deviation of ±0.08 µm).

Addition of Zn additive to the PEO bath enabled the formation of $Zn_{0.5}V_2O_4$, but only 3.1% $Zr_{0.35}Ti_{0.65}O_2$ phase, traces of $TiO_2$-rutile and significant fraction of amorphous phase at 100 V with 0.011 Hz. The quantification of oxide phases by Rietveld refinement excludes the presence of amorphous phase. EDX measurements detected oxygen content of 6.3 mass% and incorporation of 4.1 mass% Zn. The as-prepared sample exhibits a 30% lower oxygen content compared to the sample produced in absence of Zn additive (9 mass%) which have additionally 30.8% $TiO_2$-rutile phase. Addition of Zn doubles the coating's thickness to 1.98 µm (Figure 7b) with similar high homogeneity (deviation of ±0.07 µm) and visible higher porosity coherent with the lower oxygen content and high thickness. The relation of the detected fraction of oxygen with the coating's thickness indicates a significant density reduction due to zinc additive.

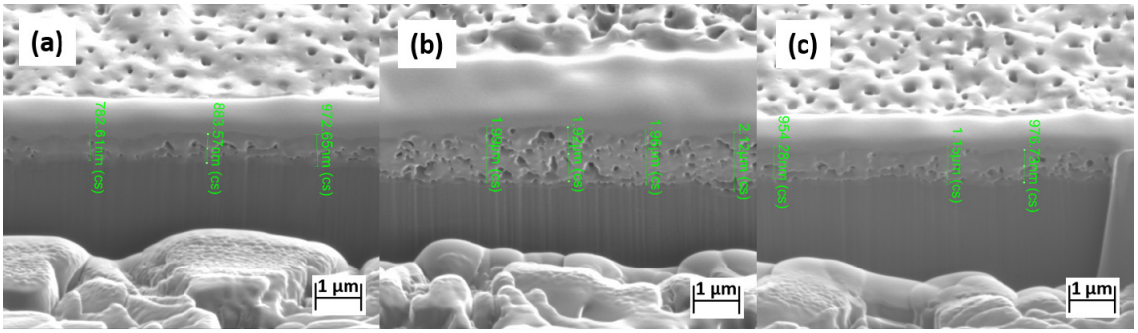


**Figure 7.** Images of FIB cross-sections of selected Ti6Al4V samples polarized at 100 V with a pulse frequency of 0.011 Hz (a) in 0.1 M sulfuric acid containing 0.12 M $Zr(SO_4)_2 \cdot H_2O$, with either (b) additional 0.03 M $ZnSO_4 \cdot 7H_2O$ or (c) 0.03 M $Cu(CH_3COO)_2 \cdot H_2O$.

In contrast to Zn, Cu additive at 100 V and 0.011 Hz (Figure 7c) led to slight increase of coating thickness (1.06 ± 0.16 µm) compared to the reference (Figure 7a). The oxygen content of 10.6 mass% and low crystalline oxide phase of 2.4 mass% indicates high amorphous phase within the PEO coating. Furthermore, 1.9 mass% Cu was detected via EDX. Figure 8 shows the change in topography and pore structure at different pulse frequencies at 150 and 200 V. The corresponding

FIB cross-sections are summarized in Figure 9. The increase of polarization voltage from 100 to 150 V (Figure 9a) at the same pulse frequency decreased the coating's thickness (0.64 µm), its homogeneity (±0.18 µm) and oxygen content (7.8 mass%). Increase of pulse frequency to 10 Hz at 150 V (Figure 9b) increased layer thickness (0.79 µm), accompanied by a minor rise in oxygen content (8.6 mass %) and slightly improved homogeneity of coating thickness (±0.17 µm). At a pulse frequency 50 Hz (Figure 9c), the coating's thickness is not further increased (0.76 µm) but the layer gains uniformity (±0.13 µm) at low oxygen content (5.3 mass%) indicating increase in porosity. Increase of polarization voltage to 200 V at 50 Hz (Figure 9c) enables growth of 0.84 µm with improved homogeneity (±0.11 µm) and an oxygen content of 6.2 mass% indicative for slightly increased density.

The varying Zr contents determined by EDX are not correlating with the XRD analysis due to inhomogeneous distribution of Zr enriched crystalline and amorphous phases within the oxide layer.

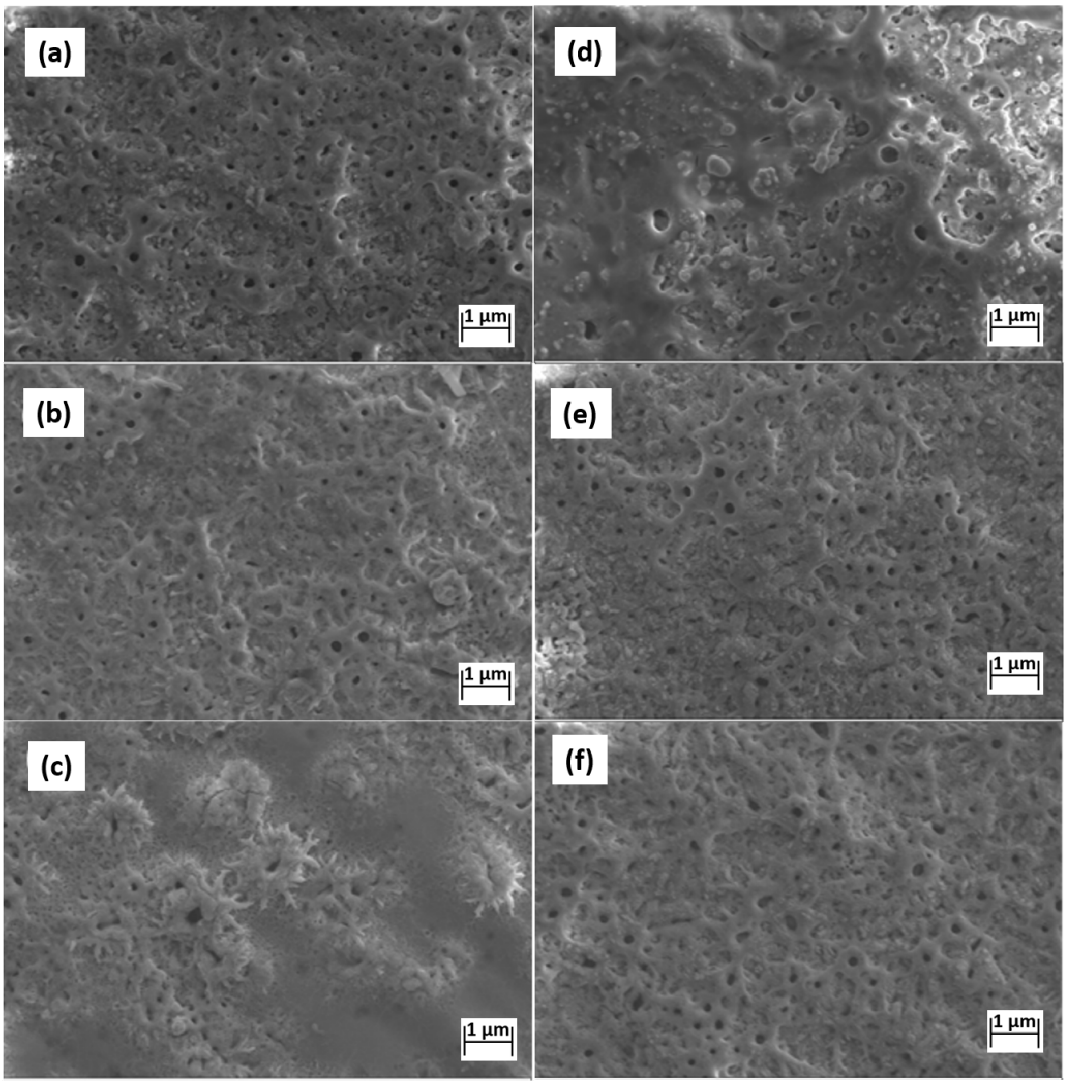


**Figure 8.** SEM images of Ti6Al4V polarized with 150 V in 0.1 M sulfuric acid containing 0.12 M $Zr(SO_4)_2 \cdot H_2O$ and 0.03 M $Cu(CH_3COO)_2 \cdot H_2O$ at different pulse frequencies: (a) 0.011 Hz, (b) 10 Hz and (c) 50 Hz, polarized with 200 V at pulse frequencies of (d) 0.011 Hz, (e) 10 Hz and (f) 50 Hz.

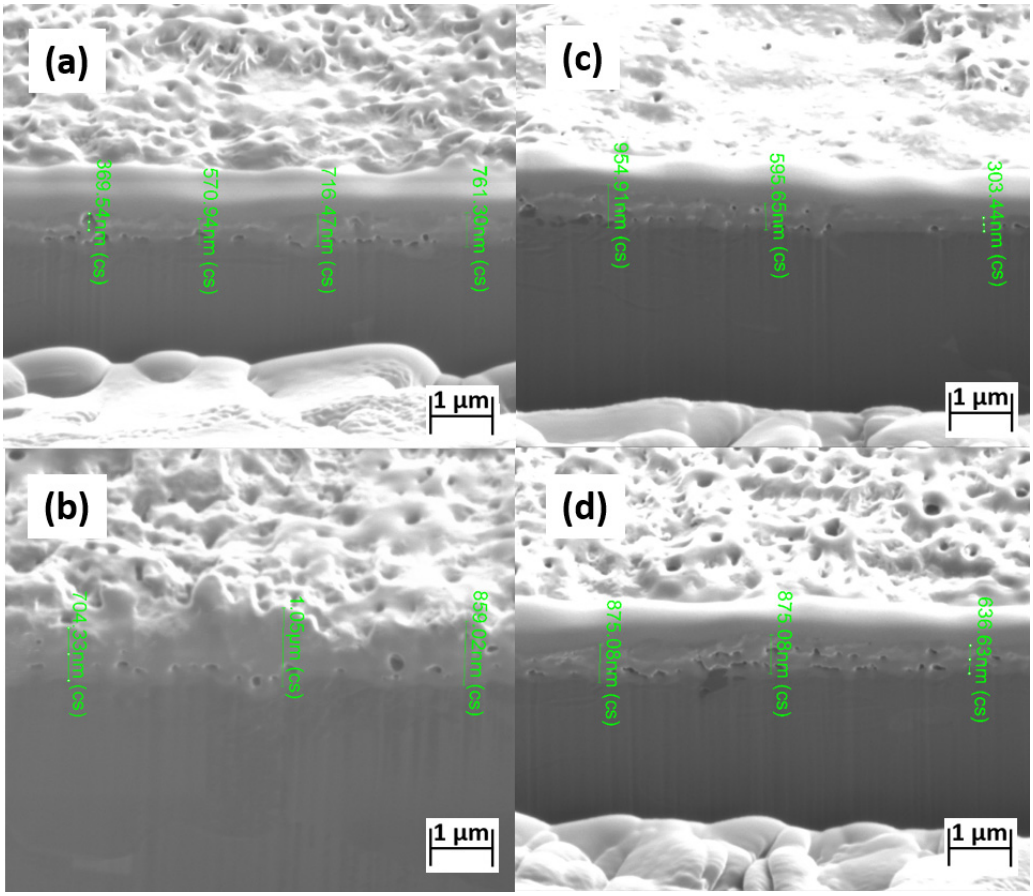


**Figure 9.** Images of FIB cross-sections of selected Ti6Al4V samples polarized in 0.1 M sulfuric acid $Zr(SO_4)_2{\cdot}H_2O$ and 0.03 M $Cu(CH_3COO)_2{\cdot}H_2O$ at 150 V with a pulse frequencies of (a) 0.011 Hz, (b) 10 Hz, (c) 50 Hz, and (d) anodized with a voltage of 200 V and 50 Hz.

The SEM imaging, EDX and XRD measurements show that the creation of a desired porous surface topography and chemistry is a balancing act between heating and quenching in order to accumulate sufficient heat for high temperature phase formation while rapidly solidifying porous structures. Variation of the pulse frequency is a powerful parameter to enlarge the working windows, enabling higher polarization voltages, but diminished the incorporation of Cu (Figure 10) and Zn. However, depending on the additives, different impactful effects alter the ceramic coating. While Zn additive restricted the working window to 100 V and enabled growth the thickest ceramic layer with low $Zr_{0.35}Ti_{0.65}O_2$ phase of the performed surface treatments, Cu additive enlarged the applicable voltage range and led to denser but thinner coatings with exclusively $Zr_{0.35}Ti_{0.65}O_2$ phase formation (Table 5).

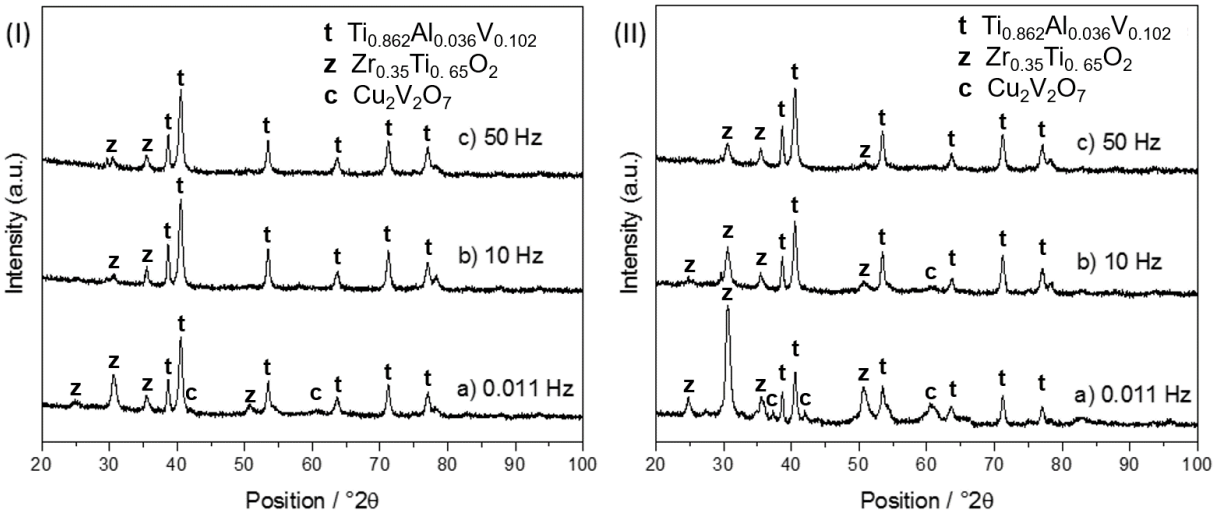


**Figure 10.** XRD patterns of Ti6Al4V treated by PEO in 0.1 M sulfuric acid containing 0.12 M $Zr(SO_4)_2 \cdot H_2O$ and 0.03 M $Cu(CH_3COO)_2 \cdot H_2O$ with voltages of 150 (I) and 200 V (II) and various frequencies of (a) 0.011 Hz (duty cycle 67%), (b) 10 Hz (duty cycle 50%) and (c) 50 Hz (duty cycle 50%).

**Table 5.** Quantification of phase composition via Rietveld refinement corresponding to Figure 10.

| Potential (V) | Pulse frequency (Hz) | $Zr_{0.35}Ti_{0.65}O_2$ (%) | $Ti_{0.862}Al_{0.036}V_{0.102}$ (%) |
|---|---|---|---|
| 150 | 0.011 | 36.9 | 63.2 |
| | 10 | 16.4 | 83.6 |
| | 50 | 10.9 | 89.1 |
| 200 | 0.011 | 80.7 | 19.3 |
| | 10 | 38.6 | 61.4 |
| | 50 | 11.6 | 88.4 |

## 4. Conclusions

In this study, the influence of different metal ion additives on the PEO coating, grown on Ti6Al4V in acidic electrolyte, was investigated.

- Addition of Zr ions led to high $TiO_2$-rutile content within the ceramic layer due to incorporation of particles precipitated from dissolved Ti in the vicinity of the substrate.
- Combination of Zr and Zn additives suppressed both phase formation of $TiO_2$-rutile and $Zr_{0.5}Ti_{0.65}O_2$ equally, but allowed fabrication of a cohesive highly porous and amorphous ceramic coating with low $Zr_{0.5}Ti_{0.65}O_2$ content and Zn incorporation.
- Combination of Zr and Cu additives shifts the occurring phase formation from $TiO_2$-rutile to the formation of $Zr_{0.5}Ti_{0.65}O_2$ phase. Depending on the polarization voltage, the $TiO_2$-rutile phase is entirely replaced by $Zr_{0.5}Ti_{0.65}O_2$. The working window is significantly increased and can be fine-tuned by variation of pulse frequency, allowing polarization voltage of at least 200 V with increased pulse frequency to create uniform porous surface topography.

- The oxide layer topography, composition and crystallinity are highly influenced by the polarization voltage and pulse frequency in potentiostatic controlled PEO. With increasing voltage, the trend to formation of the high temperature modification $Zr_{0.5}Ti_{0.65}O_2$ is apparent. Hence, the shorter the pulses the more quenching prevents heat accumulation, limits phase transition time and generates amorphous phases. Depending on the additives, the working windows vary significantly.

Both Zn and Cu additives resulted in incorporation of Zn and Cu within the surface layer, which has potential for antibacterial properties. With increasing polarization, their XRD patterns appear more pronounced and disappear with increasing frequency. The SEM images show homogeneous distribution of the pores and the FIB profiles indicate good adhesion, regularity in morphology and thickness for the coatings. Additional investigations will be required to determine both the biocompatibility and antibacterial activity of as-prepared coatings.

## Acknowledgements

These investigations were performed with the support of the Austrian Science Foundation FFG under Grant 4253627 and the government of Lower Austria and Upper Austria in the frame of the COMET program. Special thanks to Rene Wultsch for his technical support.

## Conflict of interest

There is no conflict of interests between authors.

## References

1. Ikarashi Y, Toyoda K, Kobayashi E, et al. (2005) Improved biocompatibility of titanium-zirconium (Ti–Zr) alloy: Tissue reaction and sensitization to Ti–Zr alloy compared with pure Ti and Zr in rat implantation study. *Mater Trans* 46: 2260–2267.
2. Ionita D, Pirvu C, Stoian AB, et al. (2020) The trends of TiZr alloy research as a viable alternative for Ti and Ti16 Zr roxolid dental implants. *Coatings* 10: 422.
3. Rupp F, Gittens RA, Scheideler L, et al. (2014) A review on the wettability of dental implant surfaces I: Theoretical and experimental aspects. *Acta Biomater* 10: 2894–2906.
4. Lee MH, Min BK, Son JS, et al. (2016) Kwon influence of different post-plasma treatment storage conditions on the shear bond strength of veneering porcelain to zirconia. *Materials* 9: 43.
5. Piconi C, Maccauro G (1999) Zirconia as a ceramic biomaterial. *Biomaterials* 20: 1–25.
6. Afzal A (2014) Implantable zirconia bioceramics for bone repair and replacement: A chronological review. *Mater Express* 4: 1–12.
7. Tovani CB, Ferreira CR, Simão AMS, et al. (2020) Characterization of the in vitro osteogenic response to submicron $TiO_2$ particles of varying structure and crystallinity. *ACS Omega* 5: 16491–16501.
8. Marchi J, Ussui V, Delfino CS, et al. (2010) Analysis in vitro of the cytotoxicity of potential implant materials. I: Zirconia-titania sintered ceramics. *J Biomed Mater Res B* 94: 305–311.
9. Poon KK, Wurm MC, Evans DM, et al. (2020) Biocompatibility of $(Ba,Ca)(Zr,Ti)O_3$ piezoelectric ceramics for bone replacement materials. *J Biomed Mater Res* B 108: 1295–1303.

10. Devi KB, Singh K, Rajendran N (2011) Sol-gel synthesis and characterisation of nanoporous zirconium titanate coated on 316L SS for biomedical applications. *J Sol-gel Sci Techn* 59: 513–520.
11. Polley C, Distler T, Detsch R, et al. (2020) 3D Printing of piezoelectric barium titanate-hydroxyapatite scaffolds with interconnected porosity for bone tissue engineering. *Materials* 13: 1773.
12. Gajović A, Furić K, Musić S, et al. (2006) Mechanism of $ZrTiO_4$ synthesis by mechanochemical processing of $TiO_2$ and $ZrO_2$. *J Am Ceram Soc* 89: 2196–2205.
13. Gunputh UF, Le H (2020) A review of in-situ grown nanocomposite coatings for titanium alloy implants. *J Compos Sci* 4: 41.
14. Katsui H, Goto T (2017) Bio-ceramic coating of Ca–Ti–O system compound by laser chemical vapor deposition, In: Sasaki K, Suzuki O, Takashi N, *Interface Oral Health Science 2016*, Springer, 2016: 47–62.
15. Vakili-Azghandi M, Fattah-alhosseini A, Keshavarz MK (2016) Effects of $Al_2O_3$ nano-particles on corrosion performance of plasma electrolytic oxidation coatings formed on 6061 aluminum alloy. *J Mater Eng Perform* 25: 5302–5313.
16. Mann R, Hansal WEG, Hansal S (2014) Effects of pulsed current on plasma electrolytic oxidation. *Trans Inst Met Finish* 92: 297–304.
17. Joni MS, Fattah-alhosseini A (2016) Effect of KOH concentration on the electrochemical behavior of coatings formed by pulsed DC micro-arc oxidation (MAO) on AZ31B Mg alloy. *J Alloy Compd* 661: 237–244.
18. Bayati MR, Molaei R, Kajbafvala A, et al. (2016) Investigation on hydrophilicity of micro-arc oxidized $TiO_2$ nano/micro-porous layers. *Electrochim Acta* 55: 5786–5792.
19. Malyshev VN, Volkhin AM, Gantimirov BM (2013) Tribological characteristics improvement of wear resistant MAO-coatings. *J Coat* 2013: 262310.
20. Engelkamp B, Fischer B, Schierbaum K (2020) Plasma electrolytic oxidation of titanium in $H_2SO_4$–$H_3PO_4$ mixtures. *Coatings* 10: 116.
21. Aliasghari S, Skeldon P, Thompson GE (2014) Plasma electrolytic oxidation of titanium in a phosphate/silicate electrolyte and tribological performance of the coatings. *Appl Surf Sci* 316: 463–476.
22. Fattah-Alhosseini A, Keshavarz MK, Molaei M, et al. (2018) Plasma electrolytic oxidation (PEO) process on commercially pure Ti surface: Effects of electrolyte on the microstructure and corrosion behavior of coatings. *Metall Mater Trans A* 49: 4966–4979.
23. Yao Z, Su P, Shen Q, et al. (2015) Preparation of thermal control coatings on Ti alloy by plasma electrolytic oxidation in $K_2ZrF_6$ solution. *Surf Coat Technol* 269: 273–278.
24. Sukumaran A, Rahulan N (2019) Effect of $ZrO_2$ nanoparticle coating on pure zirconium by PEO-EPD method. *AIP Conf Proc* 2134: 050009.
25. Choi JW, Kim GW, Shin KR, et al.(2017) Synthesis of zirconium–titanium oxide mixed layers on Ti substrates by plasma electrolytic oxidation and plasma-enhanced electrophoresis. *J Alloy Compd* 726: 930–938.
26. Zhang E, Li F, Wang H, et al. (2013) A new antibacterial titanium–copper sintered alloy: Preparation and antibacterial property. *Mater Sci Eng C-Mater* 33: 4280–4287.
27. Bolzoni L, Alqattan M, Peters L, et al. (2020) Ternary Ti alloys functionalised with antibacterial activity. *Sci Rep* 10: 22201.

28. Turchanin MA, Agraval PG, Abdulov AR (2008) Thermodynamic assessment of the Cu–Ti–Zr system. II. Cu–Zr and Ti–Zr systems. *Powder Metall Met Ceram* 47: 428.
29. Rokosz K, Hryniewicz T, Raaen S, et al. (2017) Development of copper-enriched porous coatings on ternary Ti–Nb–Zr alloy by plasma electrolytic oxidation. *Int J Adv Manuf Technol* 89: 2953–2965.
30. Park YJ, Song YH, An JH, et al. (2013) Cytocompatibility of pure metals and experimental binary titanium alloys for implant materials. *J Dent* 41: 1251–1258.
31. Rudnev VS, Kilin KN, Malyshev IV, et al. (2010) Plasma-electrolytic oxidation of titanium in $Zr(SO_4)_2$-containing electrolyte. *Prot Met Phys Chem Surf* 46: 704–709.
32. Troitzsch U, Christy AG, Ellis DJ (2005) The crystal structure of disordered $(Zr,Ti)O_2$ solid solution including srilankite: evolution towards tetragonal $ZrO_2$ with increasing Zr. *Phys Chem Miner* 32: 504–514.
33. Mchale AE, Roth RS (1986) Low-temperature phase relationships in the system $ZrO_2$–$TiO_2$. *J Am Ceram Soc* 69: 827–832.
34. Christoffersen R, Davies PK (1992) Structure of commensurate and incommensurate ordered phases in the system $ZrTiO_4$–$Zr_5Ti_7O_{24}$. *J Am Ceram Soc* 75: 563–569.
35. Do DB, Hung NM, Thang DV, et al. (2016) Formation of crystal structure of zirconium titanate $ZrTiO_4$ powders prepared by sol-gel Method. *J Electron Mater* 45: 2553–2558.
36. Cardoso BN, Kohlrausch EC, Laranjo MT, et al. (2019) Tuning anatase-rutile phase transition temperature: $TiO_2/SiO_2$ nanoparticles applied in dye-sensitized solar cells. *Int J Photoenergy* 2019: 7183978.
37. Zhang Y, Xiu P, Jia Z, et al. (2018) Effect of vanadium released from micro-arc oxidized porous Ti6Al4V on biocompatibility in orthopedic applications. *Colloid Surface B* 169: 366–374.
38. French RJ, Jones PJH (1993) Role of vanadium in nutrition: Metabolism, essentiality and dietary considerations. *Life Sci* 52: 339–346.
39. Heer ASK (2018) Simple and direct synthesis of zinc vanadate ($ZnV_2O_5$) nanocrystals for its electrocatalytic and antimicrobial activity. *J Chem Pharm* 9: 18–24.
40. Zhang X, Zhang Y, Chang L, et al. (2012) Effects of frequency on growth process of plasma electrolytic oxidation coating. *Mater Chem Phys* 132: 909–915.
41. Habazaki H, Uozumi M, Konno H, et al. (2003) Crystallization of anodic titania on titanium and its alloys. *Corros Sci* 45: 2063–2073.
42. Dai L, Li W, Zhang G, et al. (2017) Anti-corrosion and wear properties of plasma electrolytic oxidation coating formed on high Si content Al alloy by sectionalized oxidation mode. *IOP Conf Ser: Mater Sci Eng* 167: 012063.